

LA-UR-18-28584

Approved for public release; distribution is unlimited.

Title: Crystal Structure Evolution of U-Si Nuclear Fuel Phases as a Function of Temperature

Author(s): Vogel, Sven C.
Wilson, Tashiema Lixona
White, Joshua Taylor

Intended for: Report

Issued: 2018-09-10

Disclaimer:

Los Alamos National Laboratory, an affirmative action/equal opportunity employer, is operated by the Los Alamos National Security, LLC for the National Nuclear Security Administration of the U.S. Department of Energy under contract DE-AC52-06NA25396. By approving this article, the publisher recognizes that the U.S. Government retains nonexclusive, royalty-free license to publish or reproduce the published form of this contribution, or to allow others to do so, for U.S. Government purposes. Los Alamos National Laboratory requests that the publisher identify this article as work performed under the auspices of the U.S. Department of Energy. Los Alamos National Laboratory strongly supports academic freedom and a researcher's right to publish; as an institution, however, the Laboratory does not endorse the viewpoint of a publication or guarantee its technical correctness.

Crystal Structure Evolution of U-Si Nuclear Fuel Phases as a Function of Temperature

**Nuclear Technology
Research and Development**

***Prepared for
U.S. Department of Energy
Nuclear Technology Research and
Development Program
Advanced Fuels Campaign***

***S. C. Vogel¹,
T.L. Wilson^{1,2}, J. T. White¹
¹LANL, ²USC Columbia***



August 17, 2018

LA-UR-18-XXXXX

M3NT-18LA020201017

DISCLAIMER

This information was prepared as an account of work sponsored by an agency of the U.S. Government. Neither the U.S. Government nor any agency thereof, nor any of their employees, makes any warranty, expressed or implied, or assumes any legal liability or responsibility for the accuracy, completeness, or usefulness, of any information, apparatus, product, or process disclosed, or represents that its use would not infringe privately owned rights. References herein to any specific commercial product, process, or service by trade name, trade mark, manufacturer, or otherwise, does not necessarily constitute or imply its endorsement, recommendation, or favoring by the U.S. Government or any agency thereof. The views and opinions of authors expressed herein do not necessarily state or reflect those of the U.S. Government or any agency thereof.

SUMMARY

The crystal structure of the U_3Si_2 line compound in the U-Si system was investigated as a function of temperature from room temperature to 1373 K using high temperature neutron time-of-flight diffraction on the HIPPO diffractometer at LANSCE. The U-Si system is actively researched due to its promise as an accident tolerant nuclear fuel. The simultaneous Rietveld refinement of five histograms from the five HIPPO detector rings provided fundamental datasets for the lattice parameters, anisotropic atomic displacement parameters, and atomic positions as a function of temperature. To explore the possibility of minority phases as a result of the synthesis route and especially due to hyper-stoichiometry, a stoichiometric $\text{U}_3\text{Si}_{2.00}$ sample and a hyper-stoichiometric $\text{U}_3\text{Si}_{2.01}$ sample were studied. While minor differences in the anisotropic atomic displacement parameters between the two samples were observed, over the entire investigated temperature range no additional phases were observed. However, significant differences in the thermal expansion behavior were identified between the two compositions that warrant future investigations.

CONTENTS

SUMMARY	iii
ACRONYMS.....	ix
1. Introduction	13
2. Sample Preparation & Experimental Setup	14
3. Results	16
4. Summary and Future Work	26
5. Acknowledgements	27
6. References	27

FIGURES

- Figure 1: Schematic of the HIPPO neutron time-of-flight diffractometer. Red areas are detector panels, the blue tank is the sample chamber and the yellow device insert is the top-hat for the sample environment. 14
- Figure 2: Diffraction data (crosses) and Rietveld fit (curve) with difference curve (below) for the $U_3Si_{2.00}$ sample at room temperature (a,b) and 1025°C (c,d) for the high resolution 145° (a,c) and medium resolution 90° (b,d) detectors. The insets show the low d-spacing region of each pattern. Tick marks indicate peak positions for U_3Si_2 18
- Figure 3: Diffraction data (crosses) and Rietveld fit (curve) with difference curve (below) for the $U_3Si_{2.01}$ sample at room temperature (a,b) and 1100°C (c,d) for the high resolution 145° (a,c) and medium resolution 90° (b,d) detectors. The insets show the low d-spacing region of each pattern. Tick marks indicate peak positions for U_3Si_2 19
- Figure 4: Diffraction data (crosses) and Rietveld fit (curve) with difference curve (below) for the long count time runs for $U_3Si_{2.00}$ (8:41 hours, a,b) and $U_3Si_{2.01}$ (12:00 hours, c,d) samples for the high resolution 145° (a,c) and medium resolution 90° (b,d) detectors. The insets show the low d-spacing region of each pattern. Tick marks indicate peak positions for U_3Si_2 (lower row) and the vanadium sample container. 20
- Figure 5: Visualization of the refined crystal structures of the $U_3Si_{2.00}$ (a) and $U_3Si_{2.01}$ (b) samples including anisotropic atomic displacement parameters. Overlaid with the crystal structure are the difference Fourier maps for ~60% of the maximum density (yellow positive difference, blue negative difference). 21
- Figure 6: Lattice parameters and unit cell volumes as a function of temperature for stoichiometric $U_3Si_{2.00}$ (red) and hyper-stoichiometric $U_3Si_{2.01}$ (blue). The error bars are smaller than the data markers. Lattice parameters and unit cell volume were fitted with a 2nd order polynomial with $R^2 > 0.997$ 22
- Figure 7: Thermal expansion of the unit cell volume, the a and the c axis as a function of temperature. Note the offset of the volume expansion data for clarity. The data marked as “Ref” is from Obbard et al. (2018) for $U_3Si_{2.00}$ 22
- Figure 8: Anisotropic coefficients of thermal expansion as a function of temperature calculated using the Thermal Expansion Visualizing (TEV) program. 23
- Figure 9: Linear thermal expansion coefficient of stoichiometric $U_3Si_{2.00}$ (red) and hyper-stoichiometric $U_3Si_{2.01}$ (blue). 24
- Figure 10: Anisotropic atomic displacement parameters U_{ij} as a function of temperature. U_{11} and U_{33} correspond to atomic displacement along the a and c axes, respectively. Note the different scale for site 1. 24
- Figure 11: Ratio of U_{11}/U_{33} as a function of temperature for each atoms in $U_3Si_{2.00}$ and $U_3Si_{2.01}$ 25
- Figure 12: Bond lengths as a function of temperature. Because the bond lengths accumulate the uncertainties for lattice parameters and atomic positions, the error bars are large. 25
- Figure 13: Relative change of the bond lengths (thermal strain) as a function of temperature. 26

TABLES

Table 1: Temperatures at which diffraction data were collected.	16
Table 2: R_{wp} values resulting from the Rietveld refinements with GSAS.	17

ACRONYMS

AECL	Atomic Energy of Canada Limited
APS	Advanced Photon Source
AFC	Advanced Fuel Cycle
ANDE	Advanced Non-destructive Examination
ATF	Accident Tolerant Fuel
ATR	Advanced Test Reactor
BWR	Boiling Water Reactor
CCD	Charge-Coupled Device
CEA	French Alternative Energies and Atomic Energy Commission
CT	Computed Tomography
DOE	Department of Energy
DOE/NE	Department of Energy/Nuclear Energy program
DOT	Department of Transportation
EBS	Ethylene bis-stearate
ENDF	Evaluated Nuclear Data File
EPMA	Electron Probe Microanalysis
ERNI	Energy-resolved Neutron Imaging
FCCI	Fuel Cladding Chemical Interaction
FCMI	Fuel Cladding Mechanical Interaction
FCRD	Fuel Cycle Research and Development
FOV	Field of View
FP5	Flight-path 5 (imaging beam line at LANSCE)
FR	Fast Reactor
HEU	Highly Enriched Uranium
HFEF	Hot Fuels Examination Facility
HI	High Intensity
HIPPO	High Pressure/Preferred Orientation neutron diffractometer
IAEA	International Atomic Energy Agency
ICP-MS	Inductively coupled plasma mass spectrometry
IMCL	Irradiated Materials Characterization Laboratory
INL	Idaho National Laboratory
JAEA	Japan Atomic Energy Agency
LANL	Los Alamos National Laboratory

LANSCCE	Los Alamos Neutron Science Center
LEU	Low enriched uranium
Linac	Linear Accelerator
LWR	Light Water Reactor
MA	Minor Actinides
MAMOX	Minor Actinide bearing Mixed Oxide Fuels
MCP	Multi-channel plate
MOX	Mixed Oxide Fuels
NDE	Non-Destructive Evaluation
ND-PIE	Non-Destructive Post Irradiation Examination
NNDC	National Nuclear Data Center (at Brookhaven National Laboratory)
NPDF	Neutron Powder Diffractometer/Neutron Pair Distribution Function
NRC	Nuclear Regulatory Commission
NRC	National Research Council Canada
NRS	Neutron Resonance Spectroscopy
NRTA	Neutron Resonance Transmission Analysis
NSLS	National Synchrotron Light Source
ORNL	Oak Ridge National Laboratory
O/M	Oxygen-to-Metal ratio
PCMI	Pellet Cladding Mechanical Interaction
PIE	Post Irradiation Examination
pRAD	Proton Radiography
PSI	Paul Scherrer Institute
PWR	Pressurized Water Reactor
RE	Rare Earth element
ROI	Region of Interest
SEM	Scanning Electron Microscopy
SMARTS	Spectrometer for Materials Research at Temperature and Stress
TFRE	Transmutation Fuel with Rare earth inclusions
TMRS	Target-Moderator-Reflector System
TEM	Transmission Electron Microscopy
TOF	Time-of-flight
UN	Uranium nitride
U-Si	Uranium silicide (unspecified stoichiometry)

US

United States

CRYSTAL STRUCTURE EVOLUTION OF U-SI NUCLEAR FUEL PHASES AS A FUNCTION OF TEMPERATURE

1. Introduction

Nuclear fuel for Light Water Reactors (LWR) continues to be researched to further improve safety and optimize performance with the ultimate goal to develop Accident Tolerant Fuels (ATF). Research in this field is conducted world-wide, e.g. in Japan (Kurata, 2016), Korea (Kim et al., 2016), and in the United States (Zinkle et al., 2014, Karoutas et al., 2018). In present power reactors, uranium dioxide is the most common nuclear fuel form. Uranium compounds such as uranium silicides provide an increase in uranium density ($11.3\text{g(U)}/\text{cm}^3$ in U_3Si_2 *vis.* $9.7\text{g(U)}/\text{cm}^3$ for UO_2 , Middleburgh et al., 2016) while also improving thermal conductivity at operating temperature, thus decreasing temperature gradients between the fuel center-line and outer surface of a fuel pellet which in turn will reduce thermally-induced stresses that ultimately may lead to cracking. Lower temperature within the pellet will also reduce diffusion and thereby retard species transport and in-pile restructuring. This enhanced resistance to radiation-induced amorphization and swelling was documented by Birtcher et al. (1989, 1996) and Finlay et al. (2004). In the United States, industry led teams collaborate for this research with national laboratories and universities and the research presented here was done in a collaboration between Westinghouse Electric Company, Idaho National Laboratory, and Los Alamos National Laboratory.

For the U-Si system, Domagala (1986) provided a phase diagram with stoichiometric compounds U_3Si , U_3Si_2 , USi , U_3Si_5 , USi_2 , and USi_3 . Development of synthesis routes for U_3Si_2 were reported (Harp et al., 2015, Johnson et al., 2016, Ortega et al., 2016) as well as detailed characterizations of fresh (e.g. Berche et al., 2009, White et al., 2015, Carvajal-Nunez et al., 2018) and irradiated (e.g. Rest & Hofman, 1994, Finlay et al., 2004, Kim et al., 2009, Kim et al., 2011, Gan et al., 2011, Miao et al., 2018a) U_3Si_2 fuel forms. The material behavior under accident scenarios, e.g. loss of coolant accidents (LOCA, Miao et al., 2018b), reactivity initiated accidents (Yanagisawa et al., 1993), or in air (Wood et al., 2017) and H_2O (Nelson et al., 2018, Wood et al., 2018) environments were also studied.

However, despite the tetragonal U_3Si_2 structure being the archetype of an entire class of crystal structures, crystallographic studies on U_3Si_2 are sparse, especially when compared to the body of research on UO_2 : Remschnig et al. (1992) reviewed U-Si structures and systematically synthesized and characterized the crystal structures. Birtcher et al. (1989, 1996) and Richardson et al. (1994) utilized neutron diffraction to study the crystal structure evolution and amorphization of U_3Si_2 during neutron irradiation (one of the few diffraction characterizations of irradiated or spent fuels). Kniess et al. (2010) and Garcia et al. (2013) reported X-ray diffraction quantitative phase analysis of U_3Si_2 fuels analyzed by Rietveld analysis. More recently, Obbard et al. (2018) reported the anisotropic thermal expansion of the U_3Si_2 crystal lattice using neutron diffraction up to 1873K, but the data quality did not allow for detailed crystallographic analysis.

This study aims at closing this gap by investigating the crystal structure of U_3Si_2 to temperatures up to 1373K. This information will allow to verify the proposed phase diagrams and assess the anisotropy of the thermal expansion to estimate thermally induced stresses. Such experimental data also benchmarks simulations of the crystal structure or the phase equilibria at different temperatures. Middleburgh et al. (2016) utilized density functional theory calculations and thermomechanical analysis to assess the stability of U_3Si_2 with respect to non-stoichiometry reactions. They predict that U_3Si_2 is a line compound at room temperature, with excess Si forming Si-rich precipitates such as U_5Si_4 or USi , and stoichiometries between $\text{U}_3\text{Si}_{1.97}$ (at 1260K) and $\text{U}_3\text{Si}_{2.03}$ (at 1840K) being possible only at high temperatures, limited by defect concentrations. Detecting the predicted minority phases also motivated this work.

2. Sample Preparation & Experimental Setup

Specimens of U_3Si_2 ($\text{U}_3\text{Si}_{2.00}$ and $\text{U}_3\text{Si}_{2.01}$) were prepared by arc-melting the constitutive metals of (depleted, e.g. <0.2 atom % ^{235}U , rest ^{238}U) uranium and silicon in a tri-arc system (5TA Reed Tri-Arc, Centorr Vacuum Industries, USA) as described by White et al. (2015). High purity depleted uranium plate was used along with 99.999% pure Si (Cerac Inc.) which was melted five times using two electrodes to minimize volatilization of the Si metal. An Ar gas stream was initially purified by a Cu getter to decrease the oxygen contamination from ~ 10 ppm O_2 to 1×10^{-12} ppm O_2 prior to the arc-melting setup. Furthermore, the third electrode in the tri-arc system was used to melt Ti as an internal getter to remove additional oxygen impurities in the Ar gas stream that was not removed by the external Cu getter. The molten Ti decreased the oxygen levels to $\sim 1 \times 10^{-15}$ ppm O_2 . Oxygen levels were monitored during the arc melting process by oxygen sensors (Rapidox 3100 OEM, Cambridge Sensotec, UK) placed on the inlet and outlet of the tri-arc system. The ~ 5 g ingot of U_3Si_2 was comminuted using a mortar and pestle and sieved between a -200 and -325 mesh sieves. Processing of the powders was done within an Ar glove box line, which is maintained below 30 ppm O_2 . Annealing of the powders was conducted in a W-mesh metal furnace at 1523 K for 20 hours in a gettered argon atmosphere, with the powders subsequently loaded into vanadium sample cans (see below) within the glove box.

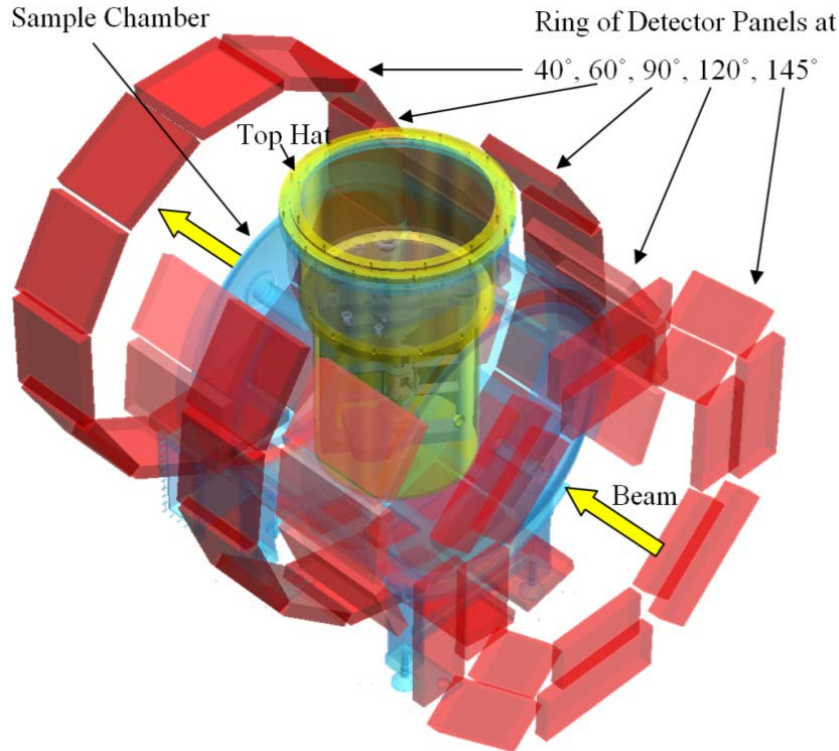


Figure 1: Schematic of the HIPPO neutron time-of-flight diffractometer. Red areas are detector panels, the blue tank is the sample chamber and the yellow device insert is the top-hat for the sample environment.

Neutron diffraction data were collected on the High Pressure/Preferred Orientation (HIPPO) neutron time-of-flight diffractometer (Wenk et al., 2003, Vogel et al., 2004) at the pulsed neutron spallation source at the Los Alamos Neutron Science Center (LANSCE, Lisowski & Schoenberg, 2005). Figure 1 shows a schematic of the instrument with 45 detector panels arranged of five rings, utilizing a total of 1,200 ^3He detector tubes covering 26.6% of the sphere around the sample (Takajo & Vogel, 2018) to detect the fraction of the $\sim 2 \times 10^7$ n/s/cm 2 incident neutron intensity at 100 μA proton current (Ino et al. 2004) scattered by the sample. The moderator to sample distance is 8.83 m. The prepared powders were loaded into 0.95 mm

diameter vanadium cans and attached to the sample stick of an ILL-type (a furnace developed at the Institute Laue-Langevin in Grenoble specifically for neutron diffraction) high temperature vacuum furnace with vanadium heating elements and heat shields. Vanadium has a coherent scattering cross-section of 0.0184 barns (coherent scattering length of $b = -0.3824$ fm), which is negligible compared the coherent scattering cross-sections of ^{238}U (8.871 barns, $b = 8.402$ fm) and Si (2.163 barns, $b = 4.1491$ fm, all cross-sections from Sears, 1992) and therefore contribute negligible diffraction signal from sample containers and furnace.

The furnaces operates at a vacuum of $<10^{-6}$ Torr and any oxygen present is likely absorbed by the vanadium before it can reach the sample material. Neutron diffraction data were collected for 120 minutes per temperature dwell point and combined into five histograms for the HIPPO detector panels at 145° (highest resolution $\Delta d/d$, lowest count rate), 120° , 90° , 60° , and 40° (lowest resolution $\Delta d/d$, highest count rate) nominal diffraction angles. Data were collected at the temperatures listed in Table 1. Additionally, to detect any minority phases, room temperature data were collected for both samples after the high temperature furnace runs for 12:00 hours ($\text{U}_3\text{Si}_{2.01}$) and 8:41 hours ($\text{U}_3\text{Si}_{2.00}$) on the HIPPO robotic sample changer (Losko et al., 2014).

The diffraction data were analyzed using GSAS (Larson & Von Dreele, 1994) with scripts written in gsa language (Vogel, 2011). All five histograms were refined simultaneously with a d-spacing range of 0.5\AA to 3.5\AA . The use of the scripted data analysis ensures that all datasets are refined with the identical data analysis strategy. The starting crystal structure for the refinement of each room temperature dataset was taken from the U_3Si_2 crystal structure reported by Zachariasen (1949, Inorganic crystal structure database record 31648) with space group $P\frac{4}{m}bm$. Time-of-flight profile function #1 in GSAS was used. Refined parameters included 12 background parameters per histogram (GSAS background function type 1), diffractometer constants DIFC (conversion from time-of-flight to d-spacing) for all histograms except for the highest resolution 145° backscattering detector bank (essentially adjusting the sample position), lattice parameters, isotropic atomic displacement parameters, atomic position parameters, one absorption parameter per histogram, and the peak width parameter σ_1 of the peak profile function. After the refinement of these parameters, the isotropic thermal motion parameters were converted to anisotropic thermal motion parameters and their values were refined together with all other parameters. For the long runs on the robotic sample changer, the vanadium phase was introduced at this point to account for the weak signal from the sample containers. For the high temperature runs, the room temperature refinement with fixed diffractometer constants (essentially accounting for slight sample misalignment relative to the calibrated sample position) and absorption values was used as a starting point for all high temperature runs and the remaining parameters were refined. The maximum number of refined parameters was 91 for the room temperature runs and 82 for the high temperature runs (not including phase scale, lattice parameter and thermal motion parameter refined for the vanadium phase in the long runs).

The results of the crystal structure refinements for the long ambient temperature runs on the robotic sample changer, including the difference Fourier maps generated by GSAS, were visualized using the VESTA package (Momma & Izumi, 2011). For all refinements, GSAS provided routines were utilized to compute bond lengths. The lattice parameters from the Rietveld analysis were used to quantify the coefficients of thermal expansion (CTEs) as a function of temperature using the Thermal Expansion Visualization (TEV) program (Langreiter & Kahlenberg, 2015). Using TEV, 2nd order polynomial fits were applied to the error-weighted lattice parameters and unit cell volume vs temperature. These polynomials and their derivatives are used to generate the 2nd order tensor describing the thermal expansion.

As in all neutron measurements, absolute lattice parameters measured without an internal standard and determined from the peak positions, are not reliable to more than 0.1% of the absolute value. In our case, the lattice parameters of the room temperature runs in the furnace and on the sample changer deviated by 0.09% (a, $\text{U}_3\text{Si}_{2.00}$), 0.09% (c, $\text{U}_3\text{Si}_{2.00}$), -0.07% (a, $\text{U}_3\text{Si}_{2.01}$), and -0.04 (c, $\text{U}_3\text{Si}_{2.01}$) despite refining the diffractometer constants nominally accounting for sample displacement. However, relative changes e.g.

due to thermal expansion, are determined reliably. Atomic positions and thermal motion parameters, determined from the peak intensities, are reliable.

Temperature [K]	U ₃ Si _{2.00}	U ₃ Si _{2.01}
293	Heating	Heating
373	Heating	Heating
473		Cooling
573	Heating	Heating
673		Cooling
773	Heating	Heating
873		Cooling
973	Heating	Heating
1073		Cooling
1198	Heating	Heating
1223	Heating	Heating
1248	Heating	Heating
1273	Heating	Heating & Cooling
1273	Heating	Heating
1298		Heating
1323		Heating
1348		Heating

Table 1: Temperatures at which diffraction data were collected.

3. Results

Table 2 lists the R_{wp} values obtained for the Rietveld fit at each temperature. For the higher quality long runs on the sample changer the agreements are slightly worse Figure 2 and Figure 3 show the Rietveld refinements of the room temperature and highest temperature runs for the U₃Si_{2.00} and U₃Si_{2.01}, respectively. Figure 4 shows the Rietveld refinement of the long runs at ambient conditions collected with the sample changer instead of the furnace after the heating. Refinements for the 145° and 90° HIPPO detector banks are shown with the simultaneously refined data for the 120°, 60°, and 40° detector banks omitted. All refinements show excellent agreement with the U₃Si₂ crystal structure. None of the patterns show indications of any other phases. Some minor peaks visible, most readily in the difference curves to the refinements, originate from the vanadium cans used as sample containers. In the long runs, this phase was added with excellent agreement with these additional peaks. All other deviations visible in the difference curve are at locations where U₃Si₂ has peaks and therefore indicative of minor deviations in the crystal structure (e.g. atomic positions or atomic displacements parameters) or a weak preferred orientations. The latter is more likely as the signatures in the difference curve differ between different detector banks. A weak shape preferred orientation, e.g. due to plate-like particles, could explain this. Given that a total of five

histograms were refined simultaneously for each analysis (two of which are shown here), the effect of a weak preferred orientation on the structural parameters reported below can be considered negligible.

Temperature [K]	R_{wp} (%) $U_3Si_{2.00}$	R_{wp} (%) $U_3Si_{2.01}$
Sample Changer	0.0183	0.0178
293	0.0082	0.0105
373	0.0076	0.0099
473		0.0099
573	0.0072	0.0092
673		0.0093
773	0.0068	0.0088
873		0.0089
973	0.0066	0.0086
1073		0.0087
1198	0.0065	0.0086
1223	0.0065	0.0086
1248	0.0064	0.0086
1273	0.0063	0.0085
1273	0.0063	0.0086
1298		0.0086
1323		0.0086
1348		0.0086

Table 2: R_{wp} values resulting from the Rietveld refinements with GSAS.

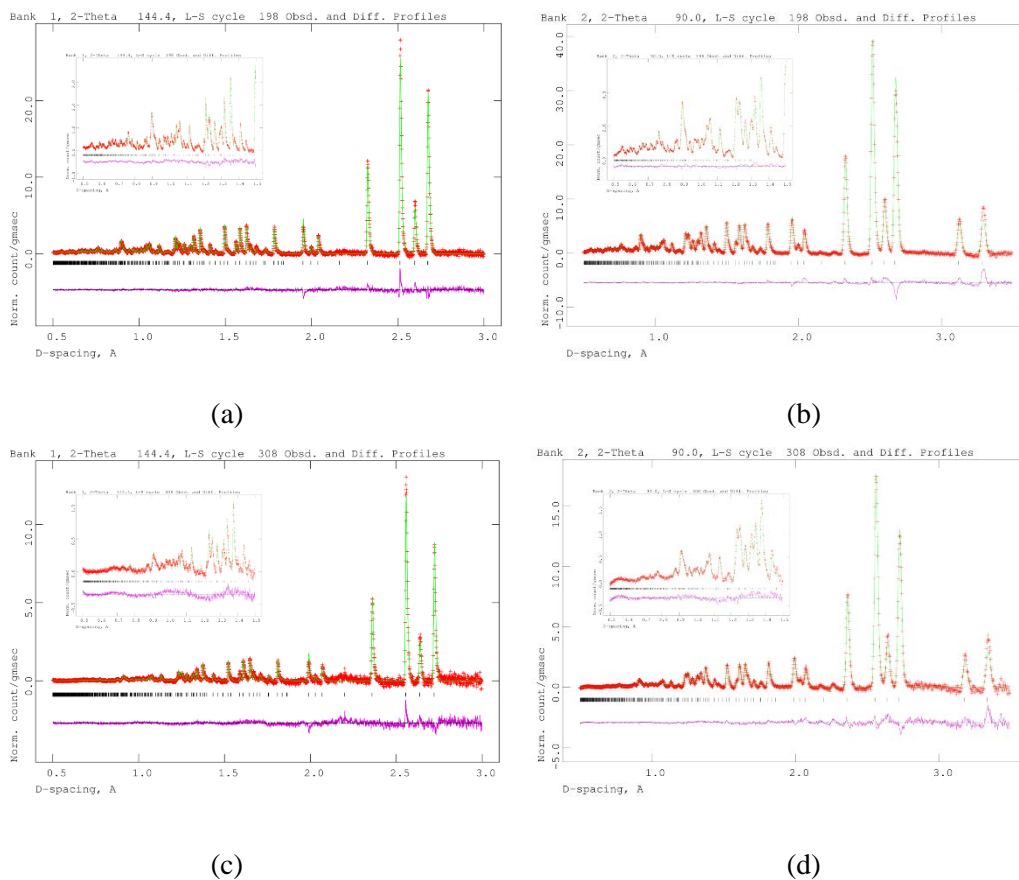


Figure 2: Diffraction data (crosses) and Rietveld fit (curve) with difference curve (below) for the $U_3Si_{2.00}$ sample at room temperature (a,b) and 1025 °C (c,d) for the high resolution 145 ° (a,c) and medium resolution 90 ° (b,d) detectors. The insets show the low d-spacing region of each pattern. Tick marks indicate peak positions for U_3Si_2 .

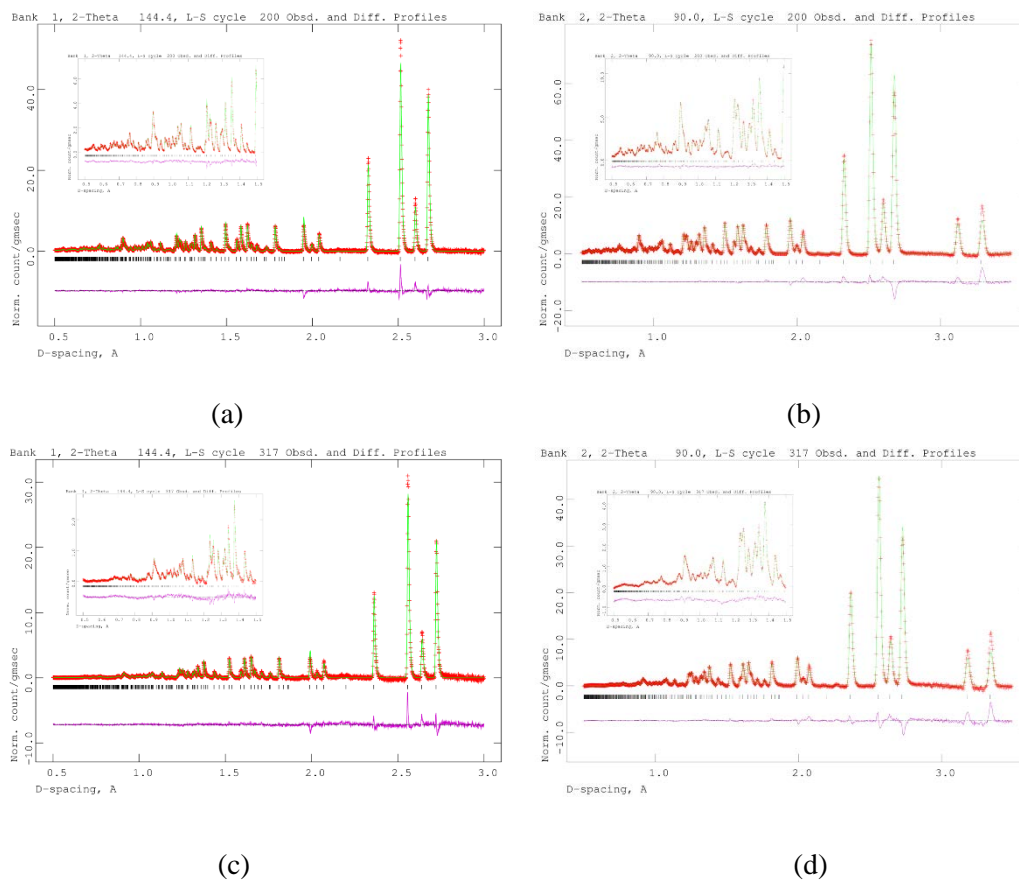


Figure 3: Diffraction data (crosses) and Rietveld fit (curve) with difference curve (below) for the $U_3Si_{2.01}$ sample at room temperature (a,b) and 1100 °C (c,d) for the high resolution 145° (a,c) and medium resolution 90° (b,d) detectors. The insets show the low d-spacing region of each pattern. Tick marks indicate peak positions for U_3Si_2 .

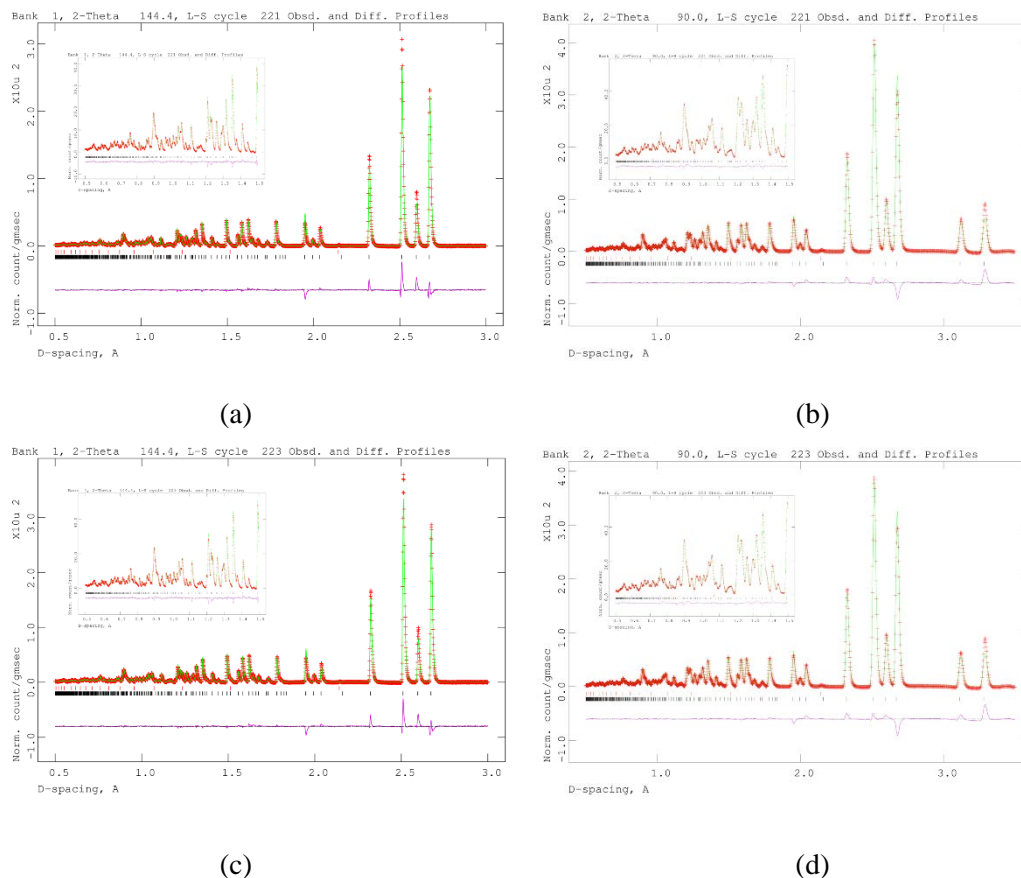


Figure 4: Diffraction data (crosses) and Rietveld fit (curve) with difference curve (below) for the long count time runs for $U_3Si_{2.00}$ (8:41 hours, a,b) and $U_3Si_{2.01}$ (12:00 hours, c,d) samples for the high resolution 145° (a,c) and medium resolution 90° (b,d) detectors. The insets show the low d-spacing region of each pattern. Tick marks indicate peak positions for U_3Si_2 (lower row) and the vanadium sample container.

Figure 5 shows the crystal structures based on the refined crystallographic parameters together with the densities above ~60% of the maximum density in the difference Fourier maps. As expected from the excellent Rietveld fits, the density distribution in the difference Fourier map does not show any major source for differences between refined parameters and data, supporting the conclusion that a mild preferred orientation is present. Anisotropic atomic displacement parameters U_{ij} are displayed as 99% probability ellipsoids (i.e. covering the entire space of possible locations). A strong anisotropy of the U1 atom, with a ~4.5 times larger amplitude of atomic displacement along the crystallographic c axis than along the a axis, is evident. The Si and U2 atoms exhibit almost isotropic atomic displacements. The refinement of the structure of the $U_3Si_{2.00}$ sample resulted in a larger atomic displacement amplitude for the U1 atom with otherwise similar results between the two compositions.

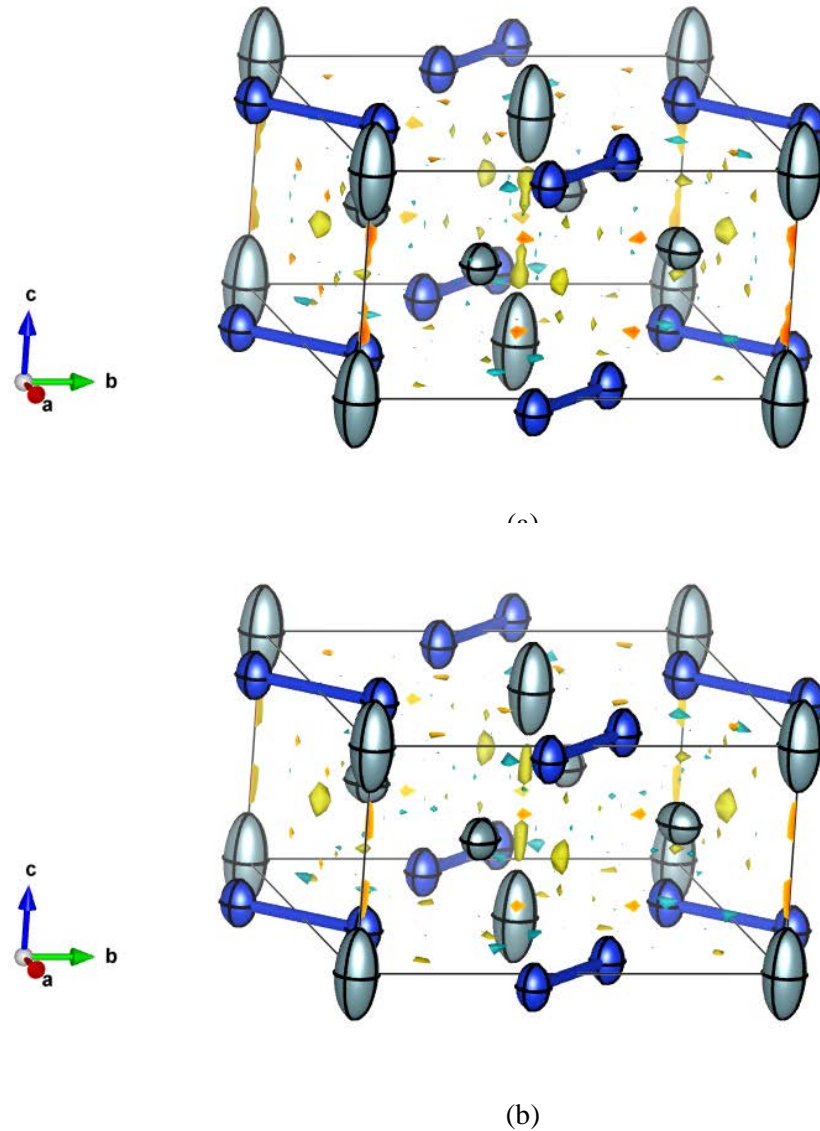


Figure 5: Visualization of the refined crystal structures of the $U_3Si_{2.00}$ (a) and $U_3Si_{2.01}$ (b) samples including anisotropic atomic displacement parameters. Overlaid with the crystal structure are the difference Fourier maps for ~60% of the maximum density (yellow positive difference, blue negative difference).

The changes in lattice parameters and unit cell volume for the two samples is shown in Figure 6. While the a lattice parameters agree within error bars, the c lattice parameters and therefore the unit cell volume for the $U_3Si_{2.01}$ sample resulted in slightly smaller values than the $U_3Si_{2.00}$ sample. While this is consistent with expectations based on lattice parameters for e.g. γ -U-Mo, where increased concentrations of the lighter elements leads to a reduced lattice parameter (Sinha et al. 2010), accurate absolute lattice parameters from neutron diffraction measurements are notoriously difficult in absence of an internal standard. The relative changes, shown in Figure 7, however, are considered accurate and allow measurement of the thermal expansion of the unit cell volume and each lattice parameter.

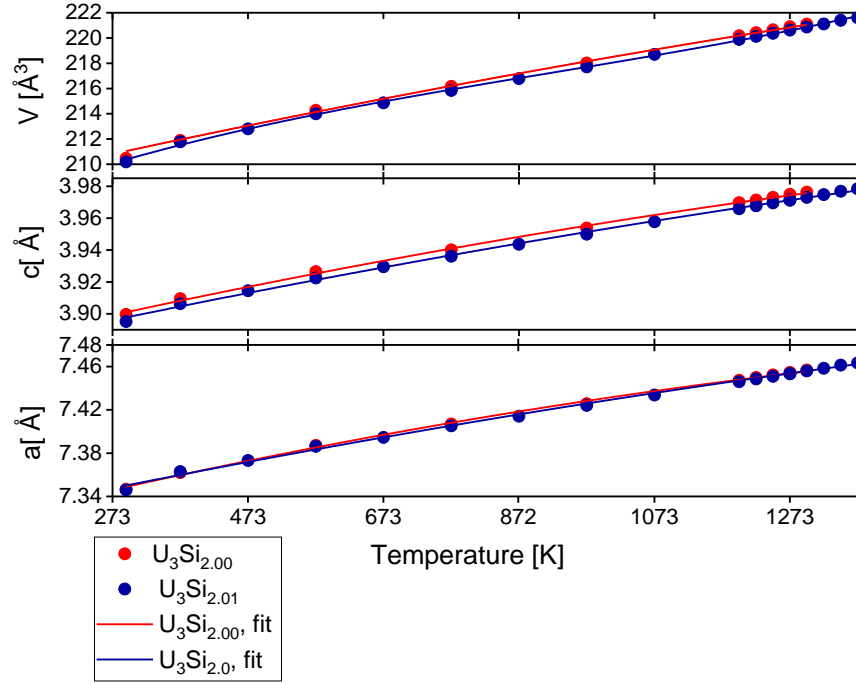


Figure 6: Lattice parameters and unit cell volumes as a function of temperature for stoichiometric $U_3Si_{2.00}$ (red) and hyper-stoichiometric $U_3Si_{2.01}$ (blue). The error bars are smaller than the data markers. Lattice parameters and unit cell volume were fitted with a 2nd order polynomial with $R^2 > 0.997$.

Using the TEV software the thermal expansion can be computed as a function of temperature for each lattice parameter as well as the unit cell volume. The results are shown in Figure 7. Overlaid are recent results by Obbard et al. (2018) for stoichiometric $U_3Si_{2.00}$. While our data agree well with those reported by Obbard et al. for the stoichiometric composition, the data obtained here for the hyper-stoichiometric $U_3Si_{2.01}$ show a smaller thermal expansion for both a and c axes compared to the stoichiometric composition.

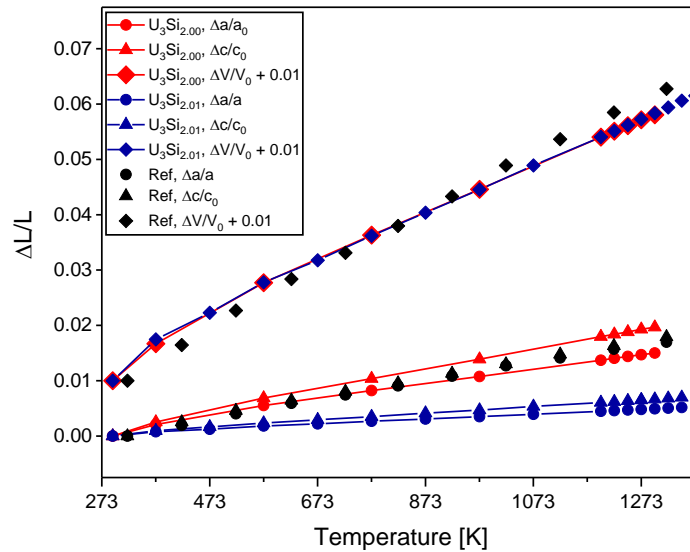


Figure 7: Thermal expansion of the unit cell volume, the a and the c axis as a function of temperature. Note the offset of the volume expansion data for clarity. The data marked as "Ref" is from Obbard et al. (2018) for $U_3Si_{2.00}$.

From the lattice parameter thermal expansion, the thermal expansion tensor can be computed as a function of temperature, also using the TEV software. The results are shown in Figure 8 and indicate that while $U_3Si_{2.00}$ expands more than $U_3Si_{2.01}$ at lower temperatures, $U_3Si_{2.00}$ expands less than $U_3Si_{2.01}$ at the higher temperatures investigated.

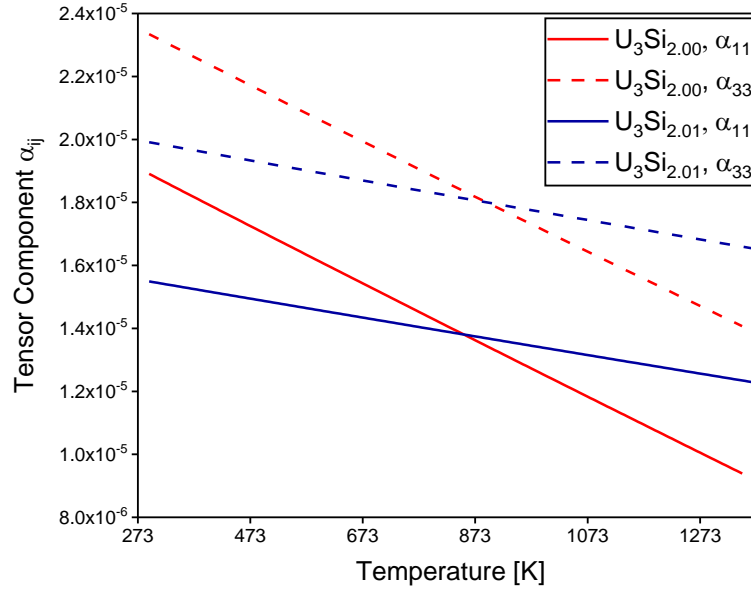


Figure 8: Anisotropic coefficients of thermal expansion as a function of temperature calculated using the Thermal Expansion Visualizing (TEV) program.

The coefficient of linear thermal expansion is related to the volumetric coefficient of thermal expansion by the equation

$$\beta(T) = 3\alpha(T) = \frac{1}{V} \frac{dV}{dT} = b_0 + b_1 T$$

where $\beta(T)$ is the volumetric coefficient of thermal expansion, $\alpha(T)$ is the linear coefficient of thermal expansion, V is volume, T is temperature and dV/dT is the change in volume with respect to temperature. By fitting the above equation and taking the local derivative of the volumetric thermal strain, the graph in Figure 9 is obtained.

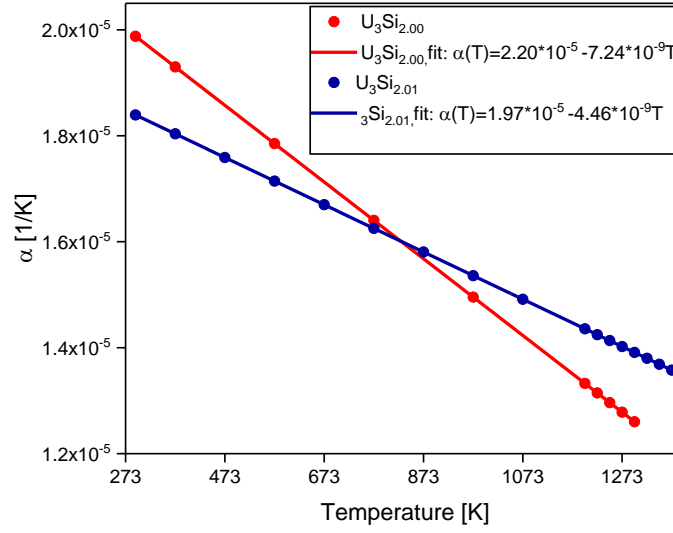


Figure 9: Linear thermal expansion coefficient of stoichiometric $U_3Si_{2.00}$ (red) and hyper-stoichiometric $U_3Si_{2.01}$ (blue).

For stoichiometric U_3Si_2 the linear thermal expansion is comparable with recent measurements made by Obbard et al. (2018), where the linear thermal expansion was calculated to be

$$\alpha(T) = 2.10 \times 10^{-5} - 7.25 \times 10^{-9}T$$

The atomic displacement parameters for the three atoms in the U_3Si_2 structure as a function of temperature are shown in Figure 10. These parameters are coupled to the phonon density of state in the system (e.g. Lane et al., 2012). The strong anisotropy of the U1 atom is evident. The ratio U_{11}/U_{33} for all atoms is shown in Figure 11 and is constant for all temperatures for atom U1, i.e. the amount of anisotropy does not vary with temperature. Both U2 and Si atoms show much more isotropic thermal displacement with only a slight preference for thermal motion along the a axis (U2) and c axis (Si), respectively. The ratio U_{11}/U_{33} for the atom U2 is also constant for the investigated temperature range, however, for the Si atom the ratio increases (i.e. becomes more isotropic) during heating and becomes slightly more anisotropic again above ~ 1200 K. While the anisotropy for the stoichiometric $U_3Si_{2.00}$ for the U1 atom is slightly higher than for the hyper-stoichiometric $U_3Si_{2.01}$, the two other atoms show only very small differences between the atomic displacement parameters. Only for the temperatures above ~ 1000 K slightly greater amplitudes for the Si atom in the stoichiometric $U_3Si_{2.00}$ were observed.

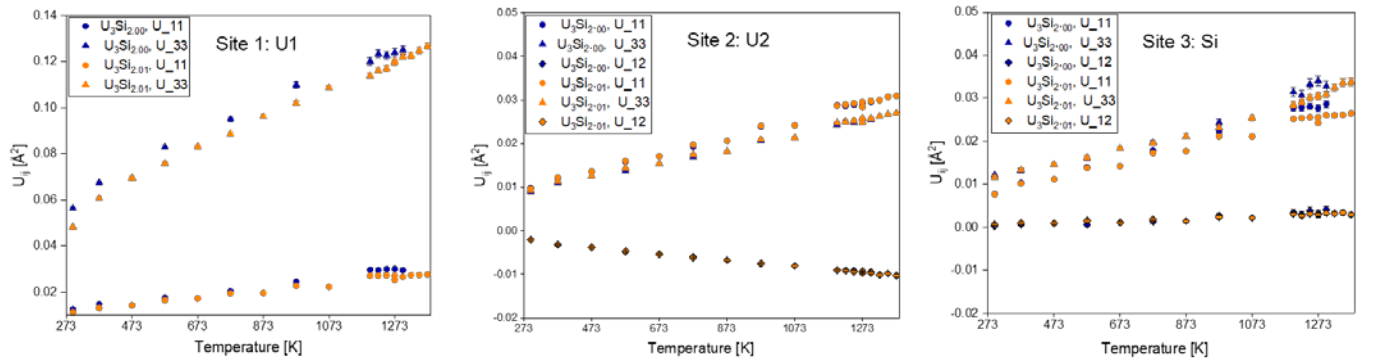


Figure 10: Anisotropic atomic displacement parameters U_{ij} as a function of temperature. U_{11} and U_{33} correspond to atomic displacement along the a and c axes, respectively. Note the different scale for site 1.

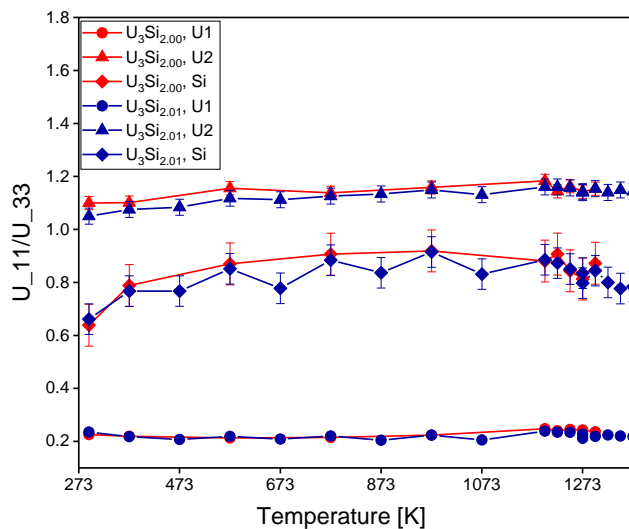


Figure 11: Ratio of U11/U33 as a function of temperature for each atoms in $U_3Si_{2.00}$ and $U_3Si_{2.01}$.

From the refined lattice parameters and atomic positions bond lengths can be computed. The absolute bond lengths as a function of temperature are shown in Figure 12. While the absolute bond lengths do not show significant trends, the plot of the relative bond length changes, or strains for each bond, shown in Figure 13, give insight into which bonds expand more than others.

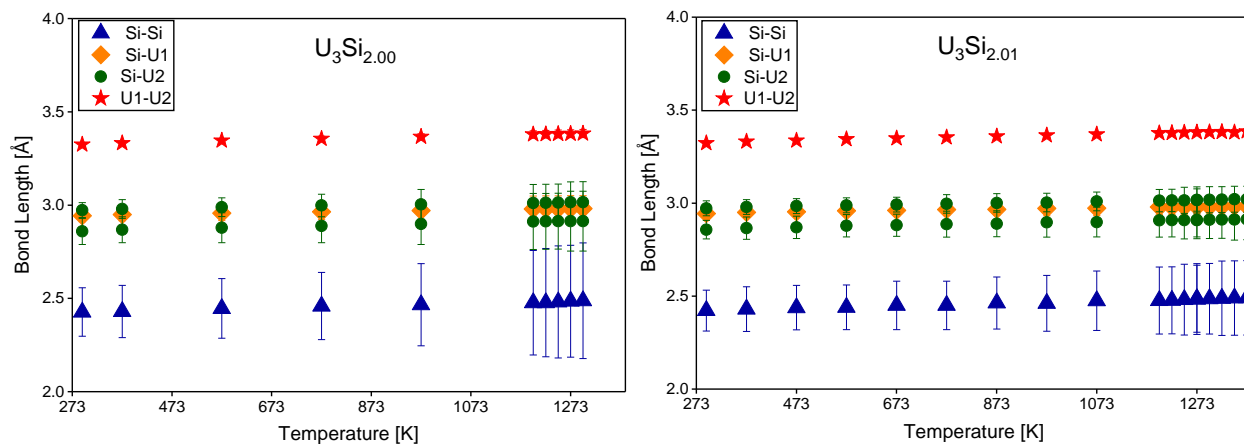


Figure 12: Bond lengths as a function of temperature. Because the bond lengths accumulate the uncertainties for lattice parameters and atomic positions, the error bars are large.

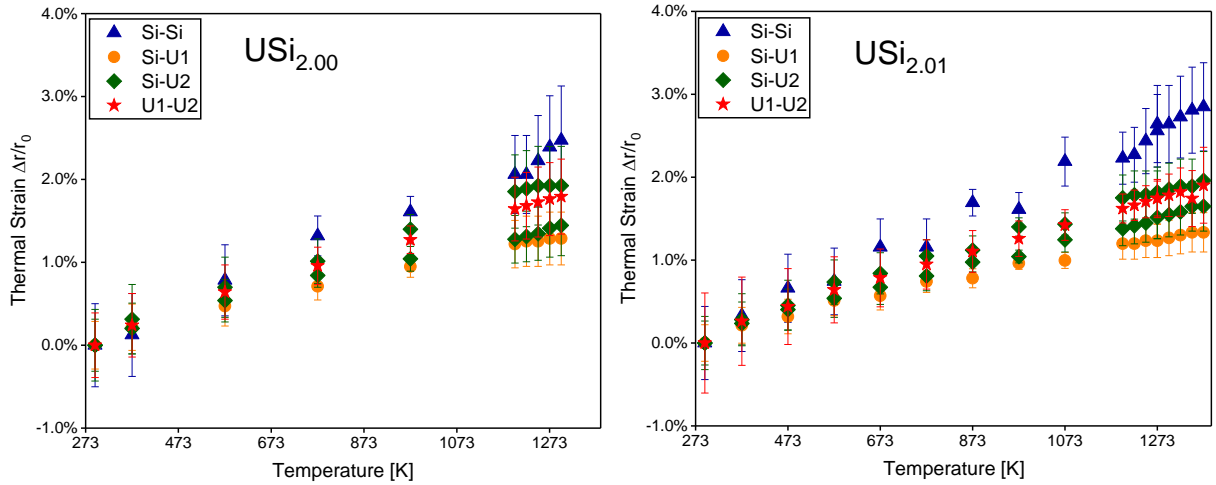


Figure 13: Relative change of the bond lengths (thermal strain) as a function of temperature.

At all temperatures and for both compositions, the Si-Si bonds show the highest relative changes with $>2\%$ at the highest temperatures investigated while the Si-U1 bonds expand by slightly more than 1%. In all cases the relative changes for the $\text{USi}_{2.01}$ is slightly higher than that of the $\text{USi}_{2.00}$. These results can be compared to simulations of the crystal structures as a function of temperature.

4. Summary and Future Work

High temperature neutron diffraction reveal changes in the crystal structure of U_3Si_2 as a function of temperature and stoichiometry. The ability of neutrons to characterize both the heavy U and the light Si atoms provides unique benefits compared to X-ray diffraction for which the diffraction signal is heavily biased towards the heavier element. Furthermore, the absence of a form factor, relevant for X-ray diffraction, provides a large d-spacing range with many reflections, which allow reliable refinement of atomic positions and atomic displacement parameters. Stoichiometric $\text{U}_3\text{Si}_{2.00}$ and hyper-stoichiometric $\text{U}_3\text{Si}_{2.01}$ were investigated over approximately the same temperature range. For both cases, no evidence for additional phases was found even in ultra-high quality data obtained in 8:41 and 12 hours. For this data quality, a detection limit of better than 0.2 wt. % is expected. The ability to fit the vanadium sample container, usually negligible for shorter runs, is evidence of this sensitivity. Good agreement for the thermal expansion of the lattice parameters and unit cell volume was found with a recent study of stoichiometric $\text{U}_3\text{Si}_{2.00}$ by Obbard et al. (2018). However, significantly different thermal expansion behavior was found for the $\text{U}_3\text{Si}_{2.01}$ sample. While absolute lattice parameters are difficult to measure with neutron diffraction, the relative changes upon which this insight is based are deemed reliable. While for both samples the anisotropic thermal motion parameters of the U1 atom site showed a significant anisotropy with ~ 4.5 times more atomic displacement along the c axis than along the a axis, only minor differences between the anisotropic thermal motion parameters were observed otherwise. Similarly, the bond lengths evolution during heating and cooling in both samples is comparable. Data for the texture analysis were collected; the analysis is ongoing and will be reported later.

While the details of the crystal structure evolution are probably most useful for benchmarking simulations, e.g. as demonstrated by Lane et al. (2012) by comparing neutron diffraction results with lattice dynamics calculations on carbide phases, the differences in thermal expansion behavior warrant future investigation as the current results indicate that thermal stresses due to CTE mismatch may occur if the chemistry changes locally. Investigations of the temperature dependent crystal structure evolution of other phases U-Si are planned and will allow detailed comparisons of thermal expansion mechanisms. The ability to detect

minority phases by exposures of several hours will be useful to compare different synthesis and processing routes.

5. Acknowledgements

This work was funded by the Fuel Cycle R&D program with the support of Kenneth J. McClellan (LANL), Heather Chichester (INL) and Steve Hayes (INL).

We gratefully acknowledge Dr. Edward Obbard for providing us with this lattice parameter data from his recent study (Obbard et al., 2018). We appreciate the thorough review of this document by Prof. John Rakovan (Miami University, Ohio). This work was supported by the US Department of Energy through the Los Alamos National Laboratory. Los Alamos National Laboratory is operated by Los Alamos National Security, LLC, for the National Nuclear Security Administration of U.S. Department of Energy (Contract DEAC52-06NA25396).

6. References

- Berche, A., Rado, C., Rapaud, O., Guéneau, C., & Rogez, J. (2009). *Journal of Nuclear Materials*, 389(1), 101-107.
- Birtcher, R. C., Mueller, M. H., Richardson, J. W., & Faber, J. (1989). *MRS Online Proceedings Library Archive*, 166.
- Birtcher, R. C., Richardson, J. W., & Mueller, M. H. (1996). *Journal of nuclear materials*, 230(2), 158-163.
- Carvajal-Nunez, U., Saleh, T. A., White, J. T., Maiorov, B., & Nelson, A. T. (2018). *Journal of Nuclear Materials*, 498, 438-444.
- Domagala, R. F. (1986). *Phases in U-Si alloys* (Report No. CONF-861185--2). Argonne National Lab.
- Finlay, M. R., Hofman, G. L., & Snelgrove, J. L. (2004). *Journal of nuclear materials*, 325(2-3), 118-128.
- Gan, J., Keiser Jr, D. D., Miller, B. D., Jue, J. F., Robinson, A. B., Madden, J. W., Medvedev, P.G. & Wachs, D. M. (2011). *Journal of Nuclear Materials*, 419(1-3), 97-104.
- Garcia, Rafael HL, Adonis M. Saliba-Silva, Elita FU Carvalho, Nelson B. Lima, Rodrigo U. Ichikawa, and Luiz G. Martinez (2013). IAEA report No. INIS-BR—14546.
- Harp, J. M., Lessing, P. A., & Hoggan, R. E. (2015). *Journal of Nuclear Materials*, 466, 728-738.
- Ino, T., Ooi, M., Kiyanagi, Y., Kasugai, Y., Maekawa, F., Takada, H., Muhrer, G., Pitcher, E.J. & Russell, G. J. (2004). *Nuclear Instruments and Methods in Physics Research Section A: Accelerators, Spectrometers, Detectors and Associated Equipment*, 525(3), 496-510.
- Johnson, K. D., Raftery, A. M., Lopes, D. A., & Wallenius, J. (2016). *Journal of Nuclear Materials*, 477, 18-23.
- Karoutas, Z., Brown, J., Atwood, A., Hallstadius, L., Lahoda, E., Ray, S., & Bradfute, J. (2018). *Progress in Nuclear Energy*, 102, 68-78.
- Kim, Y. S., Hofman, G. L., Rest, J., & Robinson, A. B. (2009). *Journal of Nuclear Materials*, 389(3), 443-449.
- Kim, Y. S., & Hofman, G. L. (2011). *Journal of Nuclear Materials*, 410(1-3), 1-9.
- Kim, H. G., Yang, J. H., Kim, W. J., & Koo, Y. H. (2016). *Nuclear Engineering and Technology*, 48(1), 1-15.

- Kniess, C. T., Carvalho, E. F. U., Durazzo, M., & Riella, H. G. (2010). IAEA report No. INIS-BE--10K0001.
- Kurata, M. (2016). *Nuclear Engineering and Technology*, 48(1), 26-32.
- Lane, N. J., Vogel, S. C., Hug, G., Togo, A., Chaput, L., Hultman, L., & Barsoum, M. W. (2012). *Physical Review B*, 86(21), 214301.
- Larson, A. C., & Von Dreele, R. B. (1986). GSAS: General structure analysis system, report LAUR 86-748. Los Alamos National Laboratory, Los Alamos, NM.
- Langreiter, T. & Kahlenberg, V. (2015). *Crystals*. 5, 143–153.
- Lisowski, P.W. & Schoenberg, K. F. (2006). *Nuclear Instruments and Methods in Physics Research Section A: Accelerators, Spectrometers, Detectors and Associated Equipment*, 562(2), 910–914.
- Losko, A. S., Vogel, S. C., Reiche, H. M. & Nakotte, H. (2014). *Journal of Applied Crystallography*, 47(6), 2109–2112.
- Miao, Y., Harp, J., Mo, K., Kim, Y. S., Zhu, S., & Yacout, A. M. (2018a). *Journal of Nuclear Materials*, 503, 314-322.
- Miao, Y., Gamble, K. A., Andersson, D., Mei, Z. G., & Yacout, A. M. (2018b). *Nuclear Engineering and Design*, 326, 371-382.
- Middleburgh, S. C., Grimes, R. W., Lahoda, E. J., Stanek, C. R., & Andersson, D. A. (2016). *Journal of Nuclear Materials*, 482, 300-305.
- Momma, K. & Izumi, F. (2011). *J. Appl. Crystallogr.* 44, 1272–1276.
- Nelson, A. T., Migdisov, A., Wood, E. S., & Grote, C. J. (2018). *Journal of Nuclear Materials*, 500, 81-91.
- Obbard, E. G., Johnson, K., Burr, P., Lopes, D. A., Gregg, D., Liss, K. D., Griffith, G., Scales, N. & Middleburgh, S. C. (2018). *Journal of Nuclear Materials*, 508, 516-520.
- Ortega, L. H., Blamer, B. J., Evans, J. A., & McDeavitt, S. M. (2016). *Journal of Nuclear Materials*, 471, 116-121.
- Remschnig, K., Le Bihan, T., Noël, H., & Rogl, P. (1992). *Journal of Solid State Chemistry*, 97(2), 391-399.
- Rest, J., & Hofman, G. L. (1994). *Journal of Nuclear materials*, 210(1-2), 187-202.
- Richardson, J. W., Birtcher, R. C., & Mueller, M. H. (1994). MRS Online Proceedings Library Archive, 373.
- Sears, V. F. (1992). *Neutron News*, 3(3), 26-37.
- Sinha, V. P., Hegde, P. V., Prasad, G. J., Dey, G. K., & Kamath, H. S. (2010). 491(1-2), 753-760.
- Sooby Wood, E., White, J. T., & Nelson, A. T. (2017). Oxidation behavior of U-Si compounds in air from 25 to 1000 C. *Journal of Nuclear Materials*, 484, 245-257.
- Sooby Wood, E., White, J. T., Grote, C. J., & Nelson, A. T. (2018). *Journal of Nuclear Materials*, 501, 404-412.
- Takajo, S., & Vogel, S. C. (2018). *Journal of Applied Crystallography*, 51(3), 895-900.
- Vogel, S. C., Hartig, C., Lutterotti, L., Von Dreele, R. B., Wenk, H. R., & Williams, D. J. (2004). *Powder Diffraction*, 19(1), 65-68.
- Vogel, S. C. (2011). *Journal of Applied Crystallography*, 44(4), 873-877.

Wenk, H.-R., Lutterotti, L. & Vogel, S. (2003). Nuclear Instruments and Methods in Physics Research Section A: Accelerators, Spectrometers, Detectors and Associated Equipment, 515(3), 575–588.

White, J. T., Nelson, A. T., Dunwoody, J. T., Byler, D. D., Safarik, D. J., & McClellan, K. J. (2015). Journal of Nuclear materials, 464, 275-280.

Yanagisawa, K., Fujuro, T., Horiki, O., Soyama, K., Ichikawa, H., & Kodaira, T. (1993). Journal of Nuclear Science and Technology, 30(8), 741-751.

Zachariasen, W. H. (1949). Acta Crystallographica, 2(2), 94-99.

Zinkle, S. J., Terrani, K. A., Gehin, J. C., Ott, L. J., & Snead, L. L. (2014). Journal of Nuclear Materials, 448(1-3), 374-379.